Iranian Journal of Science & Technology, Transaction B: Engineering, Vol. 34, No. B2, pp 179-196
Printed in The Islamic Republic of Iran, 2010

A THREE-DIMENSIONAL STUDY OF THE MOTION OF A DROP IN PLANE POISEUILLE FLOW AT FINITE REYNOLDS NUMBERS*

A. NOURBAKHSH** AND S. MORTAZAVI

Dept. of Mechanical Engineering, Isfahan University of Technology, Isfahan, 84156-83111, I. R. of Iran
Email: a.nourbakhsh@me.iut.ac.ir

Abstract– Three-dimensional simulations are presented on the motion of a neutrally buoyant drop between two parallel plates at a finite-Reynolds-number in plane Poiseuille flow, under conditions of negligible gravitational force. The full Navier-Stokes equations are solved by a finite difference/front tracking method that allows a fully deformable interface between the drop and the suspending medium and the inclusion of the surface tension. In the limit of a small Reynolds number (< 1), the direction of motion of the drop depends on the ratio of the viscosity of the drop fluid to the viscosity of the ambient fluid. At finite Reynolds numbers, the drop migrates to an equilibrium lateral position about halfway between the wall and the centerline (the Segre-Silberberg effect). Results are presented over a range of capillary number, Reynolds number, viscosity ratio and drop size. As the Reynolds number increases or capillary number or viscosity ratio decreases, the equilibrium position moves closer to the wall. The drop velocity is observed to increase with increasing capillary number and viscosity ratio, but decreases with increasing Reynolds number. The drops are more deformed with increasing the capillary number or viscosity ratio. The drop deformation increases slightly with increasing Reynolds number at constant capillary number. The equilibrium position of the three-dimensional drop is close to that predicted by two-dimensional simulations. But the translational velocities do not agree quantitatively with two-dimensional simulations.

Keywords– Drop, Poiseuille flow, finite difference/front tracking method, capillary number

1. INTRODUCTION

Motion of liquid drops and cells through narrow channels and tubes has been a matter of interest for many years and there has been a considerable interest in doing research in this area. From a practical point of view, the importance of this subject stems from many applications such as blood flow through blood vessels, the recovery of oil, the combustion of fuel sprays and emulsion transport through industrial ducts. In the present study, the motion of a three-dimensional deformable drop in a plane Poiseuille flow between two infinite parallel plates is studied by numerical simulation of the Navier-Stokes equations. Multiphase flow researchers have simulated the full time-dependent Navier-Stokes equations, but their computational modeling is limited to relatively simple systems where considerable simplifications are made in order to make simulations feasible. These approximations can be put in three categories: potential flow models for high Reynolds number flows, Stokes flow models for low Reynolds number flows, and point particle models for dilute intermediate Reynolds number flows. In contrast, the present study focuses on the migration of a three-dimensional drop at finite Reynolds numbers. The migration of neutrally buoyant solid particles in pipe flow at a finite Reynolds number was first observed by Segre & Silberberg [1, 2]. Their experimental studies showed that a rigid sphere is subject to radial forces which tend to carry

*Received by the editors April 14, 2009; Accepted November 9, 2009.
**Corresponding author

it to a certain equilibrium position at about 0.6 tube radii from the axis. Experimental studies by Karnis, Goldsmith & Mason [3, 4] showed that drops suspended in pipe flows could also exhibit the Segre-Silberberg effect. While experiments of Goldsmith & Mason used mostly a single drop and dilute suspensions, Kowalewski [5] conducted experiments on the concentrated suspension of drops and measured the concentration and velocity profiles of droplet suspensions flowing through a tube.

Theoretical studies were based on the solution of Navier-Stokes equations using perturbation methods. Ho & Leal [6] studied the inertia-induced lateral migration of a neutrally buoyant rigid sphere in a Newtonian fluid and indicated that the equilibrium position is about 0.6 of the channel half-width from the centerline for Poiseuille flow. Richardson [7] considered the behavior of a two-dimensional inviscid bubble in Stokes flow and observed that when surface tension effects are large, the cross-section of the bubble is circular.

Several numerical methods have been used in the past to study the behavior of multiphase systems in the presence of solid boundaries. These numerical methods included volume-of-fluid, Lattice-Boltzmann, finite difference, finite element and boundary-integral methods. For example, Griggs, Zinchenko & Davis [8] used a boundary-integral algorithm to study the motion of a three-dimensional drop between two parallel plates in a low-Reynolds-number Poiseuille flow and found that when deformable drops are initially placed off the centerline of the flow, the drop migrates towards the channel center. Janssen & Anderson [9] used this algorithm and modified the Green's functions to account for the effect of the walls for non-unity viscosity ratio systems. Zhou & Pozrikidis [10] simulated the pressure-driven flow of a periodic suspension of drops and showed that when the viscosity of the drops is assumed to be equal to that of the suspending fluid, the drops migrate towards the centerline of the channel. Talaie, Fathikalajahi & Taheri [11] used a three-dimensional dispersion model to investigate the effect of droplet size distribution for the prediction of liquid droplet dispersion in a venturi type scrubber. Coulliette & Pozrikidis [12] simulated the transient motion of a periodic file of three-dimensional drops in a cylindrical tube by boundary-integral method. It was found that when the capillary number is sufficiently small, the drops deform from their initial spherical shape as they migrate towards the centerline of the flow, and then approach a steady shape after a preliminary stage of rapid deformation. Feng, Ho & Joseph [13, 14] also conducted a two-dimensional finite element simulation of the motion of a solid particle in a Couette and a Poiseuille flow at finite Reynolds numbers. They observed that a neutrally buoyant particle exhibits the Segre-Silberberg effect in a Poiseuille flow. Mortazavi & Tryggvasson [15] used a finite-difference/front tracking method for numerical simulation of the motion of two-dimensional drops suspended in a pressure-driven channel flow at finite Reynolds numbers. They observed that in the limit of a small Reynolds number, the motion of the drop depends strongly on the viscosity ratio. At a higher Reynolds number, the drop moves to an equilibrium position about halfway between the centerline and the wall or it undergoes oscillatory motion.

While the numerous studies mentioned above constitute considerable progress towards understanding the low-Reynolds-number motion of drops and bubbles in channels, some important unresolved issues and computational challenges still remain. In particular, there is a need for a three-dimensional systematic assessment of the role of drop deformation on the migration of a deformable drop between two parallel plates at finite Reynolds numbers. Thus, the main goal of the current effort is to employ the finite difference/front tracking method to a three-dimensional neutrally buoyant drop between two parallel plates at finite Reynolds numbers. The simulations are performed to study the effects of capillary number, Reynolds number, viscosity ratio and drop size on the migration of the drop within the channel. Many of the features observed in the simulations are qualitatively in agreement with the experimental and numerical observations, and, in particular, with the simulations presented by Mortazavi & Tryggvason [15] for a two-dimensional deformable drop.

2. GOVERNING EQUATIONS AND NUMERICAL METHOD

a) Problem setup

The geometry of the flow is shown in Fig. 1. The motion of a drop is studied in a channel that is bounded by two flat plates in the z direction. The height and length of the channel are H. To decrease the computation time, the depth of the channel in the y-direction is taken to be $0.5H$. In absence of the drop, the undisturbed flow is driven by a constant pressure gradient (Mortazavi & Tryggvason [15]):

$$\nabla p = \nabla p_o + \nabla p' \tag{1}$$

where ∇p_o is the externally specified pressure gradient and $\nabla p'$ is the perturbation pressure gradient to be computed as part of the solution. Gravity is neglected and buoyancy effects are absent.

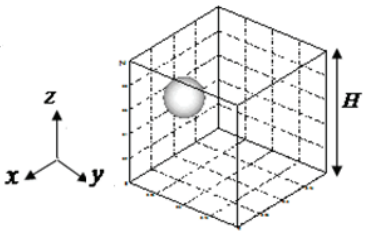

Fig. 1. The geometry for the simulation of a drop in a channel

b) Boundary conditions

The boundary condition on the plates is the no-slip condition. The domain is periodic in the x- and y-directions. Normal stresses show a jump across the interface by surface tension and tangential stresses are continuous on the surface of the drop.

c) Dimensionless parameters

The governing non-dimensional numbers are the ratio of the viscosity of the drop fluid to the suspending medium $\lambda = \mu_i / \mu_o$, the density ratio $\alpha = \rho_i / \rho_o$, and the ratio of the radius of the drop to the height of the channel $\zeta = a / H$. The viscosity and density of the drop liquid are denoted by μ_i and ρ_i, respectively, and the suspending fluid has viscosity μ_o and density ρ_o. The bulk Reynolds number is defined in terms of the undisturbed channel centerline velocity (U_c) and the channel height, as $\mathrm{Re}_b = \rho_o U_c H / \mu_o$. A Reynolds number based on the centerline velocity and the drop diameter (d) is defined by $\mathrm{Re}_d = \rho_o U_c d / \mu_o$. A particle Reynolds number can be defined as $\mathrm{Re}_p = \rho U_c a^2 / \mu H$. The capillary number, $Ca = U_c \mu_o / \sigma$, describes the ratio of the viscous stress to the interfacial tension. Non-dimensional time is defined by $\tau = t U_c / H$.

d) Numerical method

One of the important topics that has been considered by fluid mechanics researchers is flows with interfaces. Different numerical methods are used and developed for simulating these flows. These methods can be divided into two groups, depending on the type of grids used: moving grid and fixed grid. Two important approaches of fixed-grid methods, namely the volume-of-fluid (VOF) and level-set approaches, are among the most commonly used methods. The volume-of-fluid method uses a marker function. The main difficulty in using VOF method has been the maintenance of a sharp boundary between the different fluids and the computation of the surface tension. The level-set method defines the interface by a level-set function ϕ, but this approach has some difficulties in preserving the mass conservation. Another method presented in this paper is the finite difference/front tracking method which improved the disadvantages of

the previous methods. This approach was described in detail by Unverdi & Tryggvason [16,17] and only a brief outline is given here. The present computations are based on an improved implementation of the front tracking method at finite Reynolds numbers that include convective terms. The numerical technique is based on a direct discretization of the Navier-Stokes equation. In conservative form it is:

$$\frac{\partial \rho \mathbf{u}}{\partial t} + \nabla \cdot \rho \mathbf{u}\mathbf{u} = -\nabla P + \rho \mathbf{f} + \nabla \cdot \mu(\nabla \mathbf{u} + \nabla^T \mathbf{u}) + \int \sigma \kappa' \mathbf{n}' \delta^\beta (\mathbf{x} - \mathbf{x}')\, ds' \tag{2}$$

where, **u** is the velocity, P is the pressure, and ρ and μ are the discontinuous density and viscosity fields, respectively. σ is the surface tension coefficient, **f** is a body force, and surface forces are added at the interface. The term δ^β is a two- or three-dimensional δ function constructed by repeated multiplication of one-dimensional δ functions. The dimension is denoted by $\beta = 2$ or 3, κ is the curvature for two-dimensional flow and twice the mean curvature for three-dimensional flows, **n** is a unit vector normal to the front, **x** is the point at which the equation is evaluated, and x' is a Lagrangian representation of the interface.

This equation is solved by a second-order projection method using centred differences on a fixed regular, staggered grid. Both the drop and the ambient fluid are taken to be incompressible, so the velocity field is divergence free (Tryggvason et al. [18]):

$$\nabla \cdot u = 0 \tag{3}$$

Equation (3), when combined with the momentum equation, leads to a non-separable elliptic equation for the pressure. If the density is constant, the elliptic pressure equation is solved by fast Poisson solver (FISHPACK), but when the density of the drop is different from the suspending fluid, the equation is solved by a multigrid method (Adams [19]).

Equations of state for the density and the viscosity are

$$\frac{D\rho}{Dt} = 0 \quad , \quad \frac{D\mu}{Dt} = 0 \tag{4}$$

where, D/Dt is the material derivative, and equation (4) simply states that the density and the viscosity of each fluid remain constant. As the drops move, the density and the viscosity need to be updated. This is done by solving a Poisson equation for an indicator function $I(x)$ such that (Unverdi & Tryggvason [17]):

$$\rho(x) = \rho_o + (\rho_i - \rho_o) I(x) \tag{5}$$

$$\mu(x) = \mu_o + (\mu_i - \mu_o) I(x) \tag{6}$$

An indicator function that is 1 inside the drop and 0 in the outer fluid is constructed from the known position of the interface. In two-dimensional flow:

$$I(x, y) = \frac{1}{2\pi} \oint \frac{r.n}{r^2} g(r) ds \tag{7}$$

where $g(r) = 1 - e^{-r^2/\delta^2}$, and δ is a smoothness parameter.

The singularities at the front (density and viscosity gradients and surface tension) are approximated on the fixed grid by smooth functions with a compact support.

1. The structure of the front: In computations of flow containing more than one phase, the governing equations are solved on a fixed Eulerian grid, and the interface is tracked in a Lagrangian manner by a set of marker points (front) (Fig. 2). The front is represented by separate computational points that are moved by interpolating their velocity from the grid. These points are connected by triangular elements to form a

front that is used to keep the density and viscosity stratification sharp and to calculate surface tension. At each time step, information must be passed between the front and the stationary grid. This is done by a method similar to the one discussed by Unverdi & Tryggvason [16].

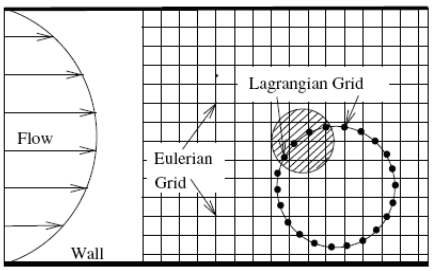

Fig. 2. The Eulerian and Lagrangian grids. From Doddi & Bagchi [20], with permission

2. Computing surface tension: The surface tension force is computed from the geometry of the interface and distributed to the grid in the same manner as the density jump. Curvature is very sensitive to minor irregularity in the interface shape, and it is difficult to achieve accuracy and robustness at the same time. However, the surface tension force is computed on each surface element by (Tryggvason et al. [18]):

$$\delta \mathbf{F}_\sigma = \sigma \int_{\delta A} k\mathbf{n}\, dA = \sigma \int_{\delta A} (\mathbf{n} \times \nabla) \times \mathbf{n}\, dA = \sigma \oint_s \mathbf{t} \times \mathbf{n}\, ds \tag{8}$$

where the integration is over the boundary curve of each element. The cross product is a vector that lies on the surface and is normal to the edge of the element. The product of the surface-tension and this vector gives the 'pull' on the edge and the net pull is obtained by integrating around the perimeter of the element.

3. RESULTS

a) Resolution tests

To ensure grid independence of the solution, resolution tests were performed at three different grid resolutions with $32\times12\times32$, $64\times24\times64$ and $128\times48\times128$ grid points. The size of the computational domain is $1\times0.375\times1$. The sensitivity of the results to mesh resolution is examined in Fig. 3, which shows the trajectory and axial velocity for a three dimensional drop at $\mathrm{Re}_d = 10$. The flow parameters are: $Ca = 0.1$, $\alpha = \lambda = 1$ and $\zeta = 0.125$. The drop is initially released close to the upper wall $(z/H = 0.825)$. The difference between the results predicted using $64\times24\times64$ and $128\times48\times128$ grids is much smaller than the difference between the results predicted using $32\times12\times32$ and $64\times24\times64$ grids. Therefore, the resolution converges with grid refinement, and grid-independent results are reached as the mesh is refined.

The flow through the gap between the drop and the wall leads to a repulsive lubrication force called 'geometric blocking' by Feng et al. [14], that pushes the drop away from the wall. The negative slip velocity and the curvature of the velocity profile generate a force that drives the drop away from the center of the channel. So, these two forces move the drop to an equilibrium position about halfway between the centerline and the wall. In Fig. 3, the equilibrium distance from the upper wall is nearly $z_{eq}/H = 0.26$ for a $64\times24\times64$ grid. The simulation for a $64\times24\times64$ grid took approximately 1800 min to reach $\tau = 125$, using an AMD Opteron(tm) Dual-Core 2216 Processor under Visual Fortran 6.

In Fig. 3, a comparison between the two- and three-dimensional simulations with the same parameters is also shown. The two-dimensional simulation was done on a 64×64 grid. The equilibrium position of the three-dimensional drop is close to that predicted by two-dimensional flow, but the three-dimensional drop has a higher axial velocity. This is due to the fact that we are considering a real drop in three-dimensional simulations, whereas in the two-dimensional case, the cylindrical sections are simulated.

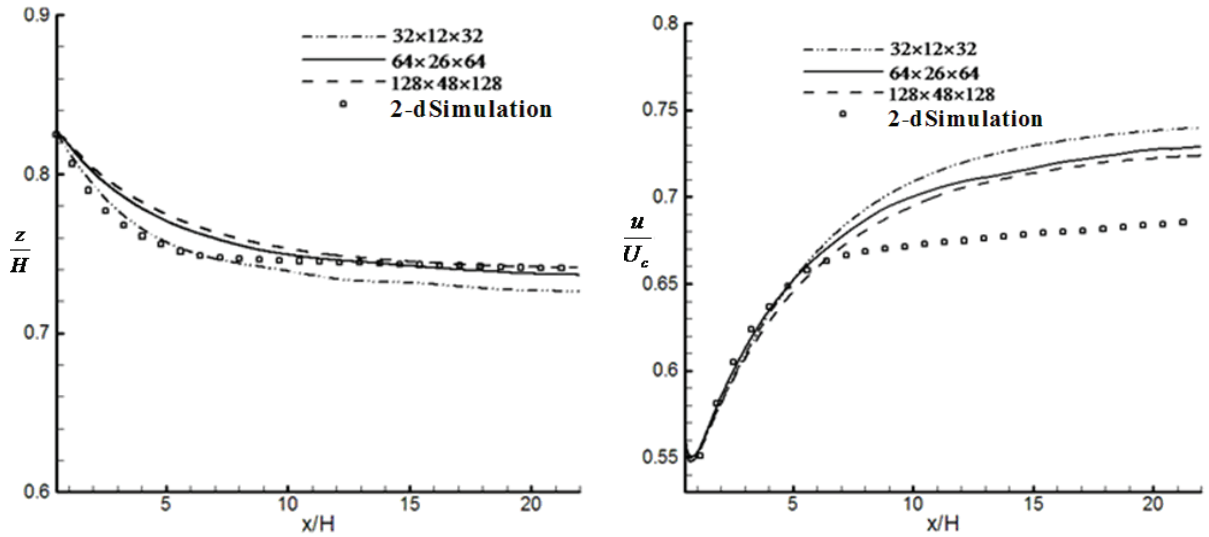

Fig. 3. Effect of resolution on the lateral migration of a drop in a plane Poiseuille flow. The lateral position and the axial velocity versus the axial location of a drop at three different grid resolutions. The two-dimensional simulation was done on a 64×64 grid. The flow parameters are: $\mathrm{Re}_d=10$, $Ca=0.1$, $\alpha=\lambda=1$ and $\zeta=0.125$

The streamlines for a three-dimensional drop are shown in Fig. 4 at the same time at two different grid resolutions with $64\times24\times64$ or $128\times48\times128$ grid points after the drop reaches an equilibrium lateral position. The flow patterns are similar.

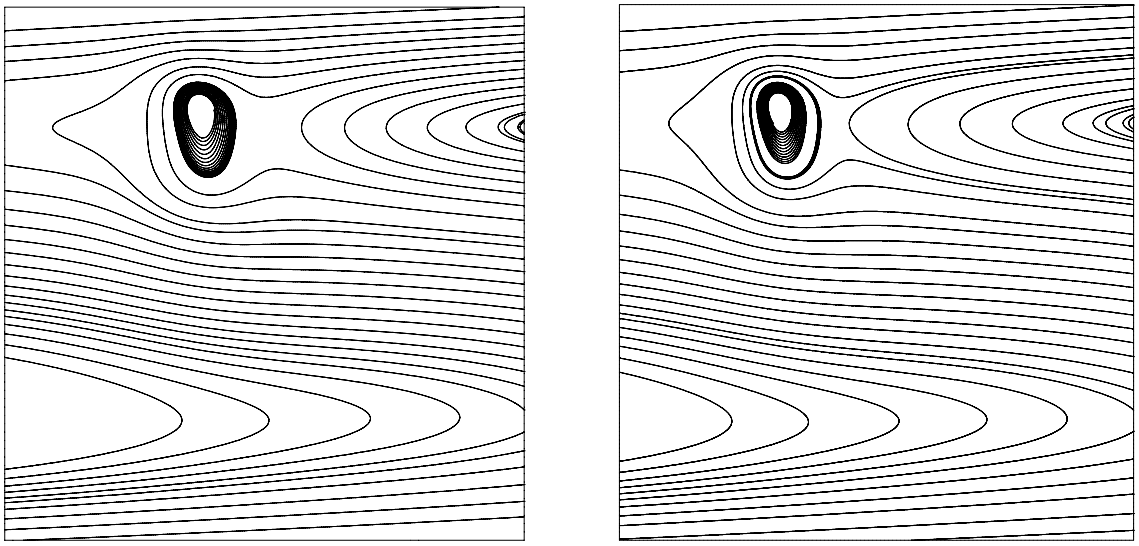

(a) (b)

Fig. 4. Streamlines for a drop at $\mathrm{Re}_d=10$, $Ca=0.1$, $\alpha=\lambda=1$ and $\zeta=0.125$ at two different grid resolutions with (a) $64\times24\times64$ and (b)$128\times48\times128$ grid points

b) Lateral migration of a liquid drop in the small inertia limit

The first study of the motion of a deformable drop in three-dimensional plane Poiseuille flow was carried out by a series of simulations in the limit of small inertia. Simulations were done with two low-Reynolds numbers: $\mathrm{Re}_d=0.25$ and $\mathrm{Re}_d=1$.

To investigate the dependence of the migration on the viscosity ratio, simulations were conducted at $\lambda=0.125$ and $\lambda=1$. The flow parameters are: $Ca=0.25$, $\alpha=1$, $\zeta=0.125$ and $\mathrm{Re}_d=0.25$. The calculations were done on a $64\times32\times64$ grid. The lateral positions of the drops are plotted versus the axial location in Fig. 5. The drop with $\lambda=0.125$ migrates towards the centerline, and the drop with $\lambda=1$

migrates away from the centerline, which is in agreement with the theoretical predictions of Chan & Leal [21] and simulations of Mortazavi & Tryggvason [15] and Zhou & Pozrikidis [10]. This result does not agree with the simulations of Griggs et al. [8], Janssen & Anderson [9] and Doddi & Bagchi [20]. The results of Griggs et al. [8] do not agree with the perturbation theory of Chan & Leal [21], who showed that for values of λ between 0.5 and 10, the drop migrates to the walls, but for $\lambda < 0.5$ and $\lambda > 10$ moves to the centerline of the channel. However, Griggs et al. [8], Janssen & Anderson [9] and Doddi & Bagchi [20] observed that the drop always migrates to the centerline of the channel at any viscosity ratio. These results do not agree with the perturbation theory of Chan & Leal [21] and are questionable.

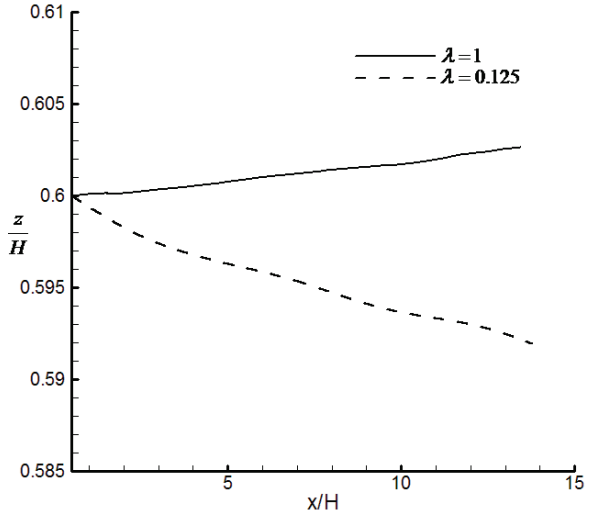

Fig. 5. The lateral position of the drops versus the axial location at $\mathrm{Re}_d = 0.25$, $Ca = 0.25$. The resolution is: $64 \times 32 \times 64$

Figure 6 shows the lateral position and the axial velocity of a drop versus the axial location at $\mathrm{Re}_d = 1$ on a $64 \times 32 \times 64$ grid. Two simulations were done with $Ca = 1$ and viscosity ratio of (a) $\lambda = 1$ and (b) $\lambda = 0.125$; and one simulation was done with $Ca = 2$ and $\lambda = 0.125$ (c). The initial positions of all drops are the same. The comparison between drops (a) and (b) shows that the low-viscosity drop (b) migrates towards the center of the channel, but the high-viscosity drop (a) migrates towards the wall. These results are again in agreement with the theory of Chan & Leal [21] for the viscosity dependence of the migration in the limit of small deformation.

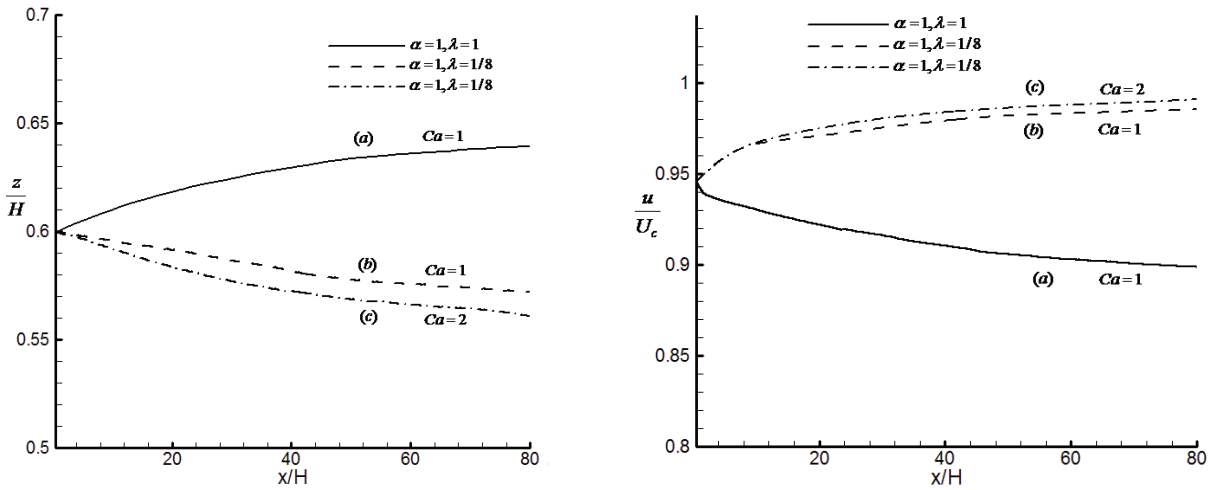

Fig. 6. Lateral position and axial velocity versus the axial position for several drops with $\mathrm{Re}_d = 1$ and different viscosity ratios

The effect of deformation on the migration of the drop can be investigated by considering drops (b) and (c) in Fig. 6, which have different capillary numbers. More deformable drop (c) migrates faster to the center of the channel.

Figure 6 shows the axial velocities of the drops versus the axial location. The comparison between drops (a) and (b) states that the axial velocity increases with decreasing viscosity ratio. This is due to the lower lateral position for the drop with lower viscosity. The result is in agreement with the simulations of Mortazavi & Tryggvason [15] for two-dimensional drops. In the present study, it is observed that as the equilibrium position moves closer to the center, the axial velocity increases, and the dimensionless axial velocity (u/U_c) will be close to one. This result is not seen in the simulation of Griggs et al. [8], who showed that the drop velocity differs from the center velocity as the equilibrium position moves closer to the center. Their results do not follow the parabolic velocity profile logically.

Figure 6 also shows that the drop with $Ca = 2$ moves slightly faster than the drop with $Ca = 1$, so the axial velocity is observed to be higher with an increasing capillary number. This is in agreement with Chan & Leal's theory [21] and the simulations of Griggs et al. [8], Doddi & Bagchi [20] and Mortazavi & Trygvason [15].

Experimental investigations on a plane Hagen-Poiseuille flow of dilute suspensions of drops with different viscosity ratios by Hiller & Kowalewski [22] showed that for low-viscosity drops $(\lambda = 0.1)$, the drop number density is highest at the centerline, but for moderate viscosity ratios $(\lambda = 1)$, the highest concentration was located between the wall and the center. This is in agreement with the simulations presented here.

c) Lateral migration of a liquid drop at moderate Reynolds numbers

In this section, the motion of a liquid drop is studied at higher Reynolds numbers, and the effects of various governing parameters are examined.

Figure 7 shows the lateral positions versus the axial location for a drop that is released at different initial positions. The flow parameters are: $\mathrm{Re}_d = 10$, $Ca = 0.05$, $\alpha = \lambda = 1$ and $\zeta = 0.125$. The calculations were done on a $64 \times 32 \times 64$ grid. This result is compared with the simulation of Feng et al. [14] at $z = 0.165H$ and $z = 0.375H$ in Fig. 7. The equilibrium position is similar to that of the two-dimensional simulations of Feng et al. [14] and the difference can be attributed to the fact that these researchers studied the rigid sphere, while we studied the deformable particle.

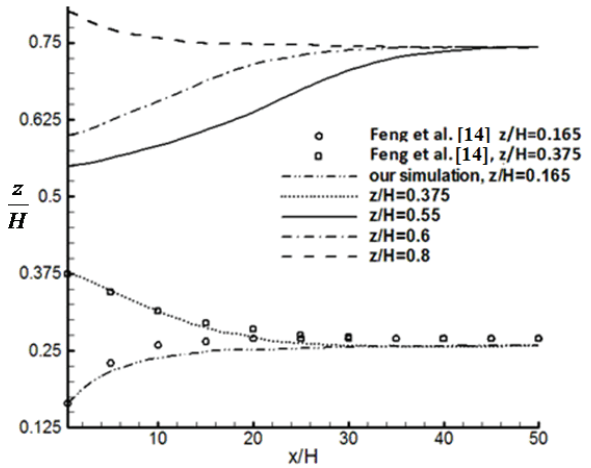

Fig. 7. Comparison of the simulated Segre-Silberberg effect with the simulation of Feng et al. [14]. The drop released at $z = 0.165H$, $z = 0.375H$, $z = 0.55H$, $z = 0.6H$, $z = 0.8H$ and $\mathrm{Re}_d = 10$ in the present study and released at $z = 0.165H$ and $z = 0.375H$ with $\mathrm{Re}_p = 0.625$, $\mathrm{Re}_b = 40$ in simulation of Feng et al. [14]

Drops that are initially close to the wall migrate towards the centerline, whereas drops that are initially close to the centerline migrate towards the wall. In the former case, the inward migration is due to the repelling effect of the wall, whereas in the latter case, the outward migration is due to the curvature in the mean velocity profile (Zhou & Pozrikidis [10]). So, all drops with different initial positions move to an equilibrium lateral position about halfway between the centerline and the wall according to the so-called Segre-Silberberg effect. The equilibrium distance from the upper wall is $z_{eq}/H = 0.25$, which is close to that predicted by two-dimensional simulations of Feng et al. [14], which showed that the equilibrium position is $z_{eq}/H = 0.252$ for a solid particle released in a plane Poiseuille flow.

Experimental investigations of Segre & Silberberg [2], Oliver [23] and the theoretical prediction of Ho & Leal [6] have shown that a sphere is subject to a radial force which tends to carry it to a certain equilibrium position between the centerline and the wall, irrespective of the radial position at which the sphere is released.

The drop gradually deforms while it migrates to the equilibrium position. Figure 8 shows computed shapes of the drops at various times for the transient migration of the drop at $Ca = 0.7$, $\mathrm{Re}_d = 10$ and $\alpha = \lambda = 1$. The drop is initially released at position $z = 0.8H$ with $\zeta = 0.125$. It initially elongates and migrates away from the upper wall ($\tau = 0.625$). The major axis of the drop is oriented at about 45° with respect to the channel wall. The drop then continues to deform more ($\tau = 0.975$), reaching the maximum, and as the time passes it decreases ($\tau = 3.375$). When the drop reaches the equilibrium position, it attains a stationary shape ($\tau = 25, \tau = 40$) and the viscous forces along the interface of the droplet due to the flow are balanced by the surface tension. This deformation will be described in section 3.c.1 at $Ca = 0.7$. These types of dynamic shapes for drops are observed for a wide range of Reynolds numbers, viscosity ratios and (subcritical) capillary numbers.

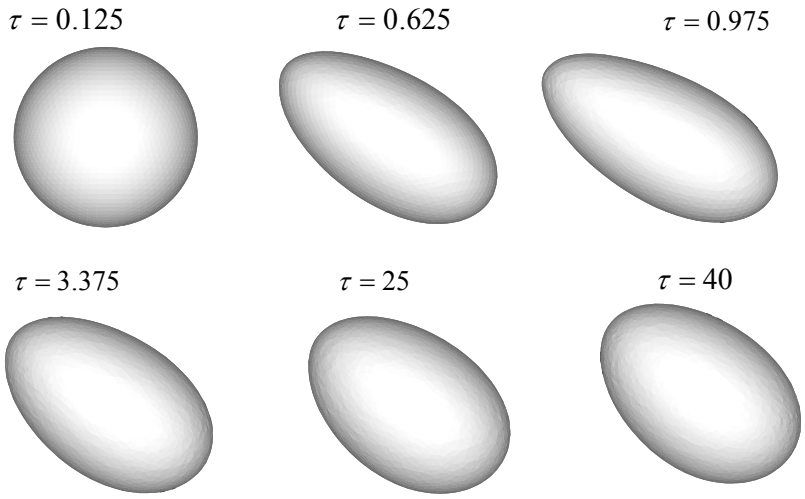

Fig. 8. The evolution of a deformable drop initially placed at $z = 0.8H$, with $\mathrm{Re}_d = 10$, $\alpha = \lambda = 1$, $\zeta = 0.125$ and $Ca = 0.7$ at various times

1. Effect of the capillary number: For drops in Stokes flow, the drop migration is only due to deformation. A spherical particle does not migrate to any direction if it is released in a flow with zero Reynolds number, so there is no lateral force for such a particle. But a deformable drop always migrates away from the walls of a channel, as it is released at a position close to the channel walls. This migration is only due to deformation and is absent for a rigid spherical particle. If the flow is at finite Reynolds number, a drop migrates to an equilibrium position at about halfway between the centerline and the wall.

The effect of deformation at higher Reynolds numbers is illustrated in Fig. 9. The streamlines at steady state are shown for drops with $Ca = 0.1$ and 0.7. Other flow parameters are: $\mathrm{Re}_d = 10$, $\alpha = \lambda = 1$

and $\zeta = 0.125$. The calculations were done on a $64 \times 32 \times 64$ grid. The flow patterns are similar, but as the capillary number is increased, the drops are more deformed and the streamlines are slightly different.

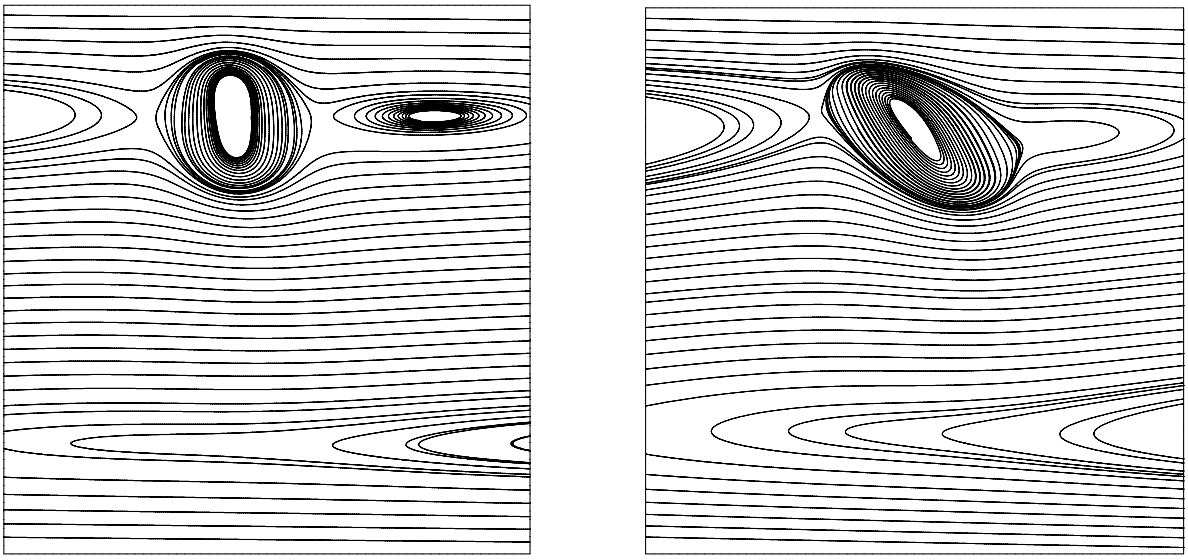

(a) (b)

Fig. 9. Streamlines for a drop at $\mathrm{Re}_d = 10$, $\alpha = \lambda = 1$ and $\zeta = 0.125$. The capillary number is 0.1 for (a) and 0.7 for (b)

The lateral position of the drop is plotted versus the axial location in Fig. 10a at $Ca = 0.1,\ 0.3,\ 0.5, 0.7$ and $\mathrm{Re}_d = 10$. It is clear that the drop migrates faster towards the channel centre with increasing capillary number (The equilibrium distance from the upper wall is $z_{eq}/H = 0.28$ for $Ca = 0.5$). Similar behaviors have been reported by Griggs et al. [8], Janssen & Anderson [9] and Doddi & Bagchi [20].

The axial velocities of the drops are plotted versus the axial location in Fig. 10b. The axial velocity increases with increasing capillary number. There is a reduction in the axial velocity in the initial transient period and can be attributed to the onset of shape distortion. Following this initial period, the axial velocity increases, owing to the streamlined shape adopted by the drop. Griggs et al. [8] and Martinez & Udell [24] found that the component of the drop velocity parallel to the walls is an increasing function of capillary number. The slip velocities, defined as the axial velocity of the drop minus the undisturbed fluid velocity at the drop center, are plotted in Fig. 10c. With increasing the capillary number, the slip velocity decreases, which is consistent with the simulations of Mortazavi & Tryggvason [15].

To describe the geometrical state of the drop, we consider the deformation parameter $D = (L-b)/(L+b)$ where L and b are, respectively, the maximum and minimum drop dimensions [25]. The deformation of the drops is plotted versus time in Fig. 10d. The drops start deforming from a spherical shape, and then reach a steady state shape. In all cases, the drops migrate to an equilibrium lateral position about halfway between the centerline and the wall in agreement with the results of Coulliette & Pozrikidis [12]. The rate of deformation is significant during the initial transient period. It is clear from Fig. 10d that the drop deformation increases with increasing capillary number due to the increase in viscous stresses along the interface. Because the previous studies constitute the zero-Reynolds-number motion of drops and bubbles, the deformation values of the drops cannot be compared with other efforts in this area. But these values are qualitatively in agreement with the observations by Griggs et al. [8], Janssen & Anderson [9] and Kang et al. [26]. Figure 11 shows the steady three-dimensional drop shapes at $Ca = 0.1,\ 0.3,\ 0.5$ and 0.7 at time 2.000122. When the capillary number is small, the drop maintains a nearly spherical shape. As the capillary number increases, the drop elongates.

The major axis of the drop is oriented at about 45° with respect to the channel wall. This result is consistent with that reported by Mortazavi & Tryggvason [15], Tsai & Miksis [27], Doddi & Bagchi [20]. Schleizer & Bonnecaze [28] also found that as the capillary number increases, the drop deforms more due to the increase in viscous stresses along the interface and, above the critical values of the capillary number, no steady shape exists.

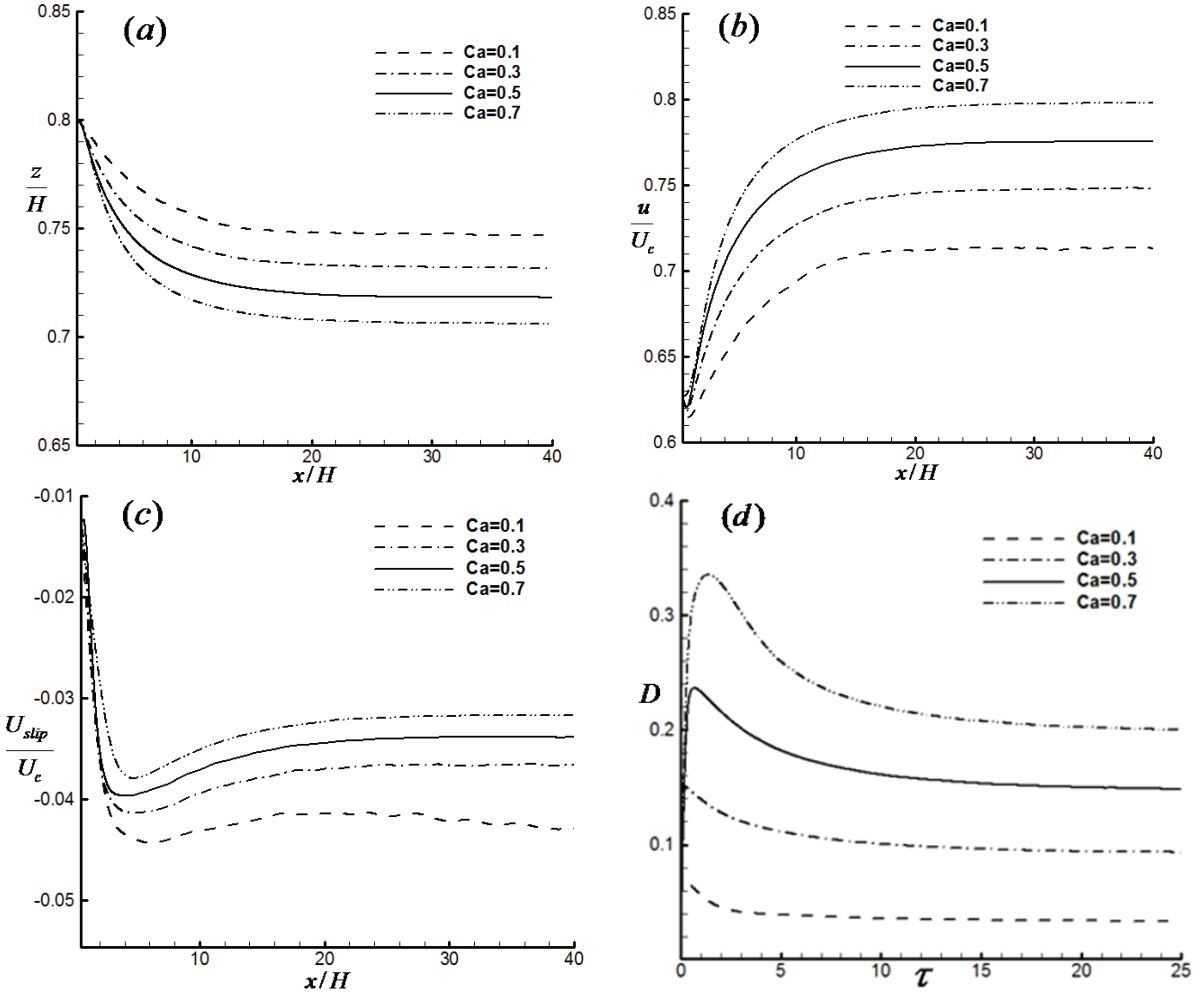

Fig. 10. (a)The lateral position, (b) axial velocity, (c) slip velocity versus the axial position and (d) drop deformation versus non-dimensional time at $\mathrm{Re}_d = 10$

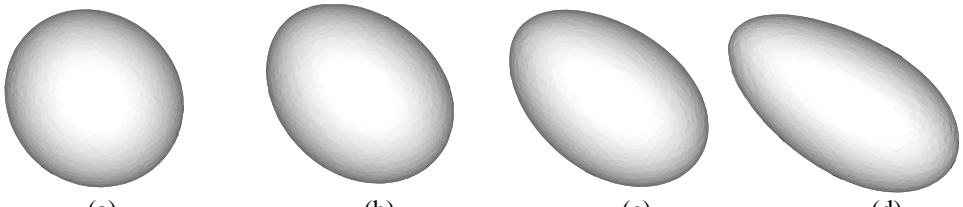

(a) (b) (c) (d)

Fig. 11. The steady-state shapes of deformable drops at $\mathrm{Re}_d = 10$, $\alpha = \lambda = 1$ and $\zeta = 0.125$, (a) $Ca = 0.1$, (b) $Ca = 0.3$,(c) $Ca = 0.5$ and (d) $Ca = 0.7$

In Fig. 12a, the lateral position of the drop is plotted versus time at $Ca = 0.2$, 0.4 and 0.8 at $\mathrm{Re}_d = 10$. It is clear that the drop migrates faster towards the channel centre with increasing capillary number. The lateral velocity of the drop is plotted versus time in Fig. 12b. The drop migrates to a lower equilibrium position with higher capillary number, therefore, its lateral velocity becomes larger. When the drop

reaches an equilibrium lateral position about halfway between the centerline and the wall, the lateral velocity becomes zero.

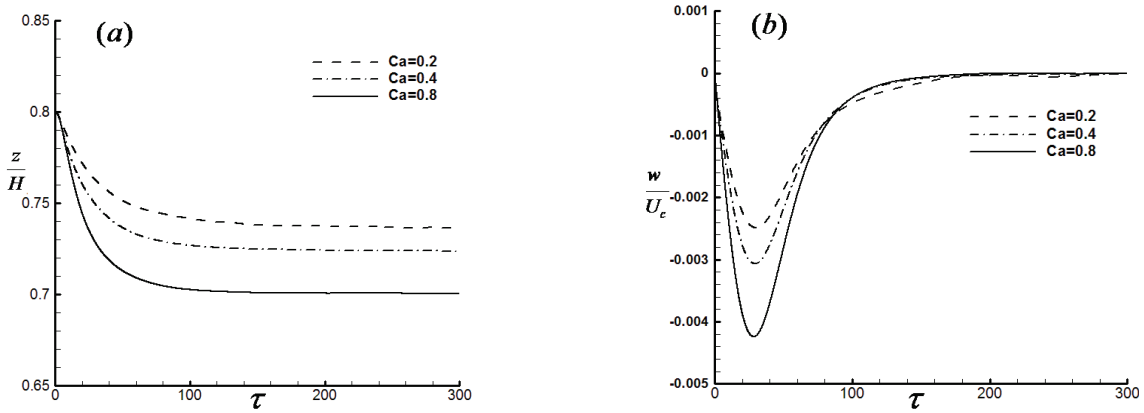

Fig. 12. (a) The lateral position and (b) lateral velocity versus non-dimensional time at three different capillary numbers

Figure 13 depicts drop shapes at $Ca = 0.8$ at various times. The flow conditions are: $\mathrm{Re}_d = 10$, $\alpha = \lambda = 1$ and $\zeta = 0.125$. The drop initially elongates in the direction of the flow and migrates away from the upper wall ($\tau = 1.00075, 3.125$). In this period, the shear rate is high, and subsequently a tail is formed at intermediate stages, which can be due to the viscous stresses that act on the interface ($\tau = 6.12525, 8.2495$). Afterwards, the tail disappears due to the smaller shear rate acting on the drop. As the drop approaches the equilibrium position, the shear rate becomes small and the drop obtains a steady shape as shown at time $\tau = 8.75$.

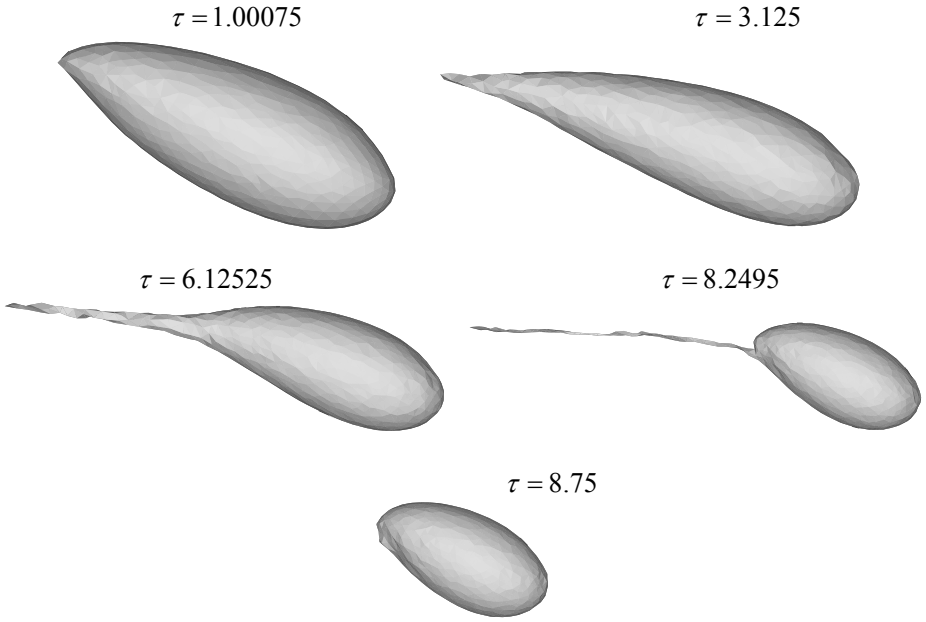

Fig. 13. The evolution of a deformable drop initially placed at $z = 0.8H$, with $\mathrm{Re}_d = 10$, $\alpha = \lambda = 1$, $\zeta = 0.125$ and $Ca = 0.8$ taken at various times

These computations show that at small values of capillary number, the drop deforms and attains a stationary shape. As capillary number is increases, the drop elongates. We find that steady-state drop shapes are obtained up to $Ca = 1$. Above this critical value of capillary number, the drop does not obtain a steady shape but instead, continuously deforms and eventually breaks up.

2. Effect of the Reynolds number: Figure 14a shows the lateral position of the drop versus the axial location for Reynolds numbers $\mathrm{Re}_d = 2.5$, 5, 10 and 15 at $Ca = 0.3$, $\alpha = \lambda = 1$ and $\zeta = 0.125$. The grid resolution is $64 \times 32 \times 64$. The drop moves to an equilibrium lateral position about halfway between the centerline and the wall according to the so-called Segre-Silberberg effect. As the Reynolds number increases, the equilibrium position moves slightly closer to the wall. The results are in agreement with those reported by Schonberg & Hinch [29], Yang et al. [30], Asmolov [31], Mortazavi & Tryggvason [15] and Segre & Silberberg [2]. The axial and slip velocities of the drops versus the axial location are shown in Fig. 14b,c. As the Reynolds number increases, the axial velocities decrease, but the slip velocities increase in agreement with the results of Yang et al. [30]. Figure 14d shows a slight increase of the drop deformation with increasing Reynolds number, however, the drop deformation is nearly the same at steady state equilibrium position.

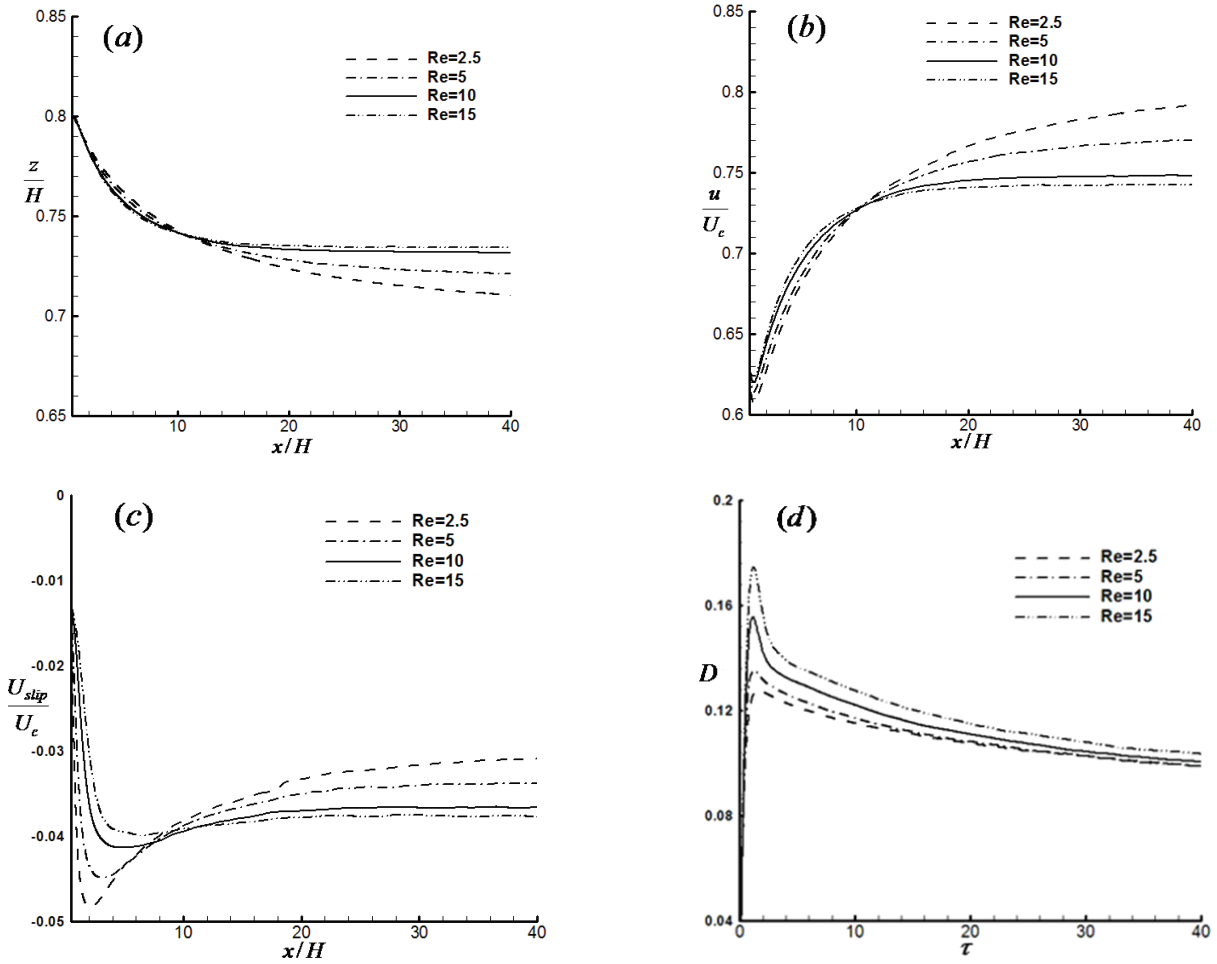

Fig. 14. (a) The lateral position, (b) axial velocity, (c) slip velocity versus the axial position and (d) drop deformation versus non-dimensional time at four different Reynolds numbers

3. Effect of the viscosity ratio: The lateral migration of a drop is affected by the ratio of the viscosity of the drop fluid to that of the suspending medium. In this section, calculations have been performed to study drop migration at different viscosity ratios for a small deformation $(Ca = 0.05)$ and moderate Reynolds numbers $(\mathrm{Re}_d = 10)$. The grid resolution is $64 \times 32 \times 64$ in the x-, y- and z-directions, respectively.

In Fig. 15a, the lateral position of the drop is plotted versus its axial location for three viscosity ratios $(\lambda = 2$, 6 and 10$)$. It is observed that the drop migrates nearly monotonically to the equilibrium position according to the Segre-Silberberg effect. The equilibrium position of low-viscosity drop is slightly closer to the wall than that of the more viscous drop, which is consistent with the Mortazavi &

Tryggvason's simulations [15]. In Fig. 15b, the axial velocity of the drop is shown versus its axial location. As the viscosity ratio increases, so does the axial velocity. This is due to a lower equilibrium position for the drop with higher viscosity. Our results differ from those of Doddi & Bagchi [20], Griggs et al. [8], Mortazavi & Tryggvason [15] and Martinez & Udell [24], who found that velocity decreases with increasing λ. This difference can be attributed to the fact that these researchers studied the creeping flow, while we studied flow at finite Reynolds numbers. The comparison between the results of section 3.b and 3.c.3 shows that variation of the equilibrium position with viscosity ratios in creeping flow is completely different from flow at finite Reynolds numbers. The drop migrates to a lower equilibrium position with higher viscosity, therefore, its axial velocity becomes larger. Figure 15c shows the maximum drop elongation as a function of time. For the range of λ considered here, the deformation for steady drop shapes increases with increasing viscosity ratio, but the trends for the dynamic deformation are not as simple. This increase is very little (less than 0.005), because the drop size and capillary number are small. In all cases, the drop initially elongates as it is deformed by the flow, and then relaxes towards a more compact steady shape. During the initial short-time elongation phase, the low-viscosity drop deforms the most rapidly (and reaches maximum elongation in the shortest time), because it offers less viscous resistance to dynamic deformation. In contrast, after the relaxation phase, high-viscosity drop reaches the greatest deformation. Since, in general, the rate of lateral migration increases with increasing deformation, the low-viscosity drop moves most rapidly towards the channel centerline during the initial phase, but higher-viscosity drop may migrate more rapidly towards the centerline during the latter phase. Similar behavior was observed by Griggs et al. [8], Martinez & Udell [24], Schleizer & Bonnecaze [28] and Janssen &Anderson [9] for Stokes flow.

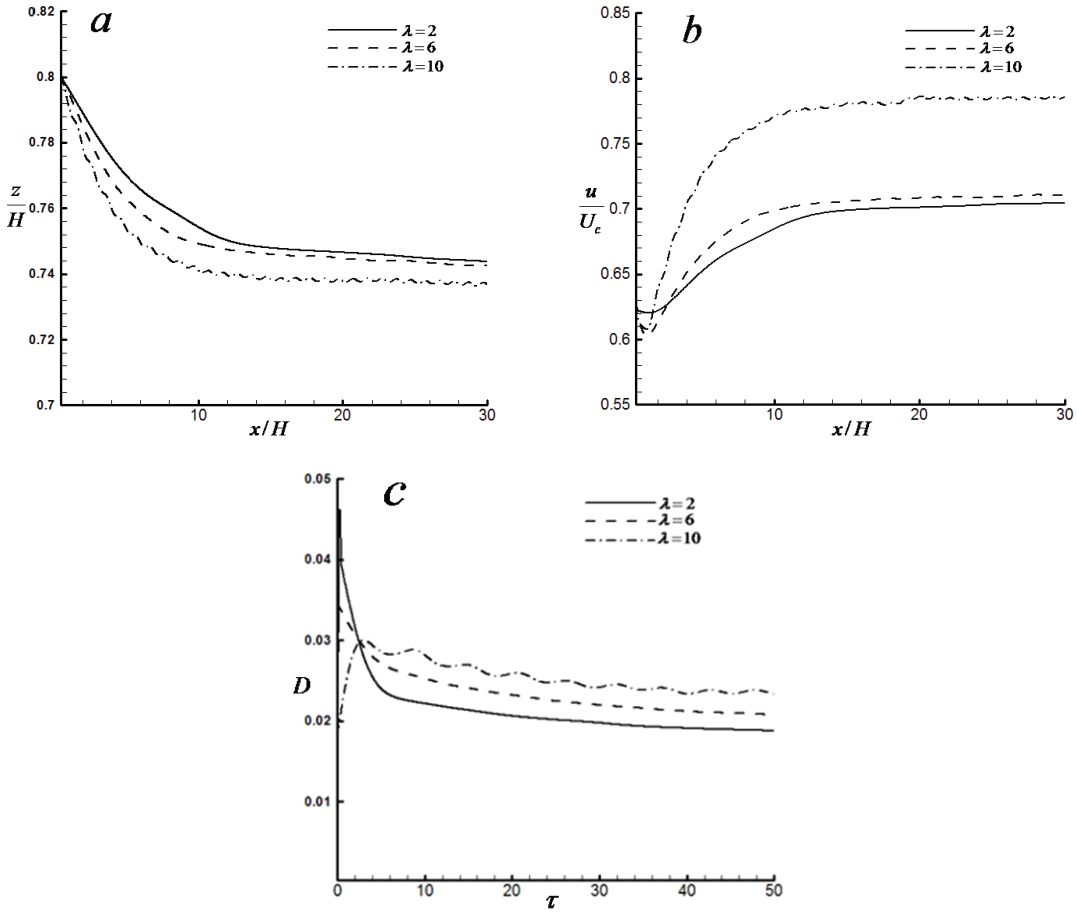

Fig. 15. (a) The lateral position, (b) axial velocity versus the axial position and (c) drop deformation versus non-dimensional time at three different viscosity ratios

4. Effect of the drop size: In Fig. 16a, the lateral position of the drop is plotted versus the axial position for three drops with different sizes. The flow conditions are: $\mathrm{Re}_d = 10$, $Ca = 0.05$, $\alpha = \lambda = 1$ and $\zeta = 0.09,\ 0.1875,\ 0.25$. The drop is initially released at $z = 0.55H$. The size of the computational domain is $1 \times 0.6875 \times 1$ and the grid resolution is $64 \times 44 \times 64$ in the x-, y- and z-directions, respectively. With increasing the radius of the drop, the centroid of the drop moves away from the wall. This is due to the fact that a larger lubrication force results for the larger drop. This force moves the drop further away from the wall. Similar phenomenon was observed by Mortazavi & Tryggvason [15], Yang et al. [30] and Karnis et al. [4]. Figure 16b depicts the axial velocity of a drop as a function of axial position for three drops with different sizes. The axial velocity decreases with increasing the size of the drop, which is consistent with the findings of Martinez & Udell [24] and Griggs et al. [8]. The deformation of three drops is shown in Fig. 16c as a function of time. The degree of deformation increases with increasing the radius of the drop. As the area of the drop increases, the effect of the upper plate becomes increasingly more important because more fluid is pushed through a smaller gap, requiring a greater local pressure gradient and increasing deformation. Schelizer & Bonnecaze [28], Doddi & Bagchi [20] and Martinez & Udell [24] showed that as the size of the droplet increases, the deformation of the drop increases as well.

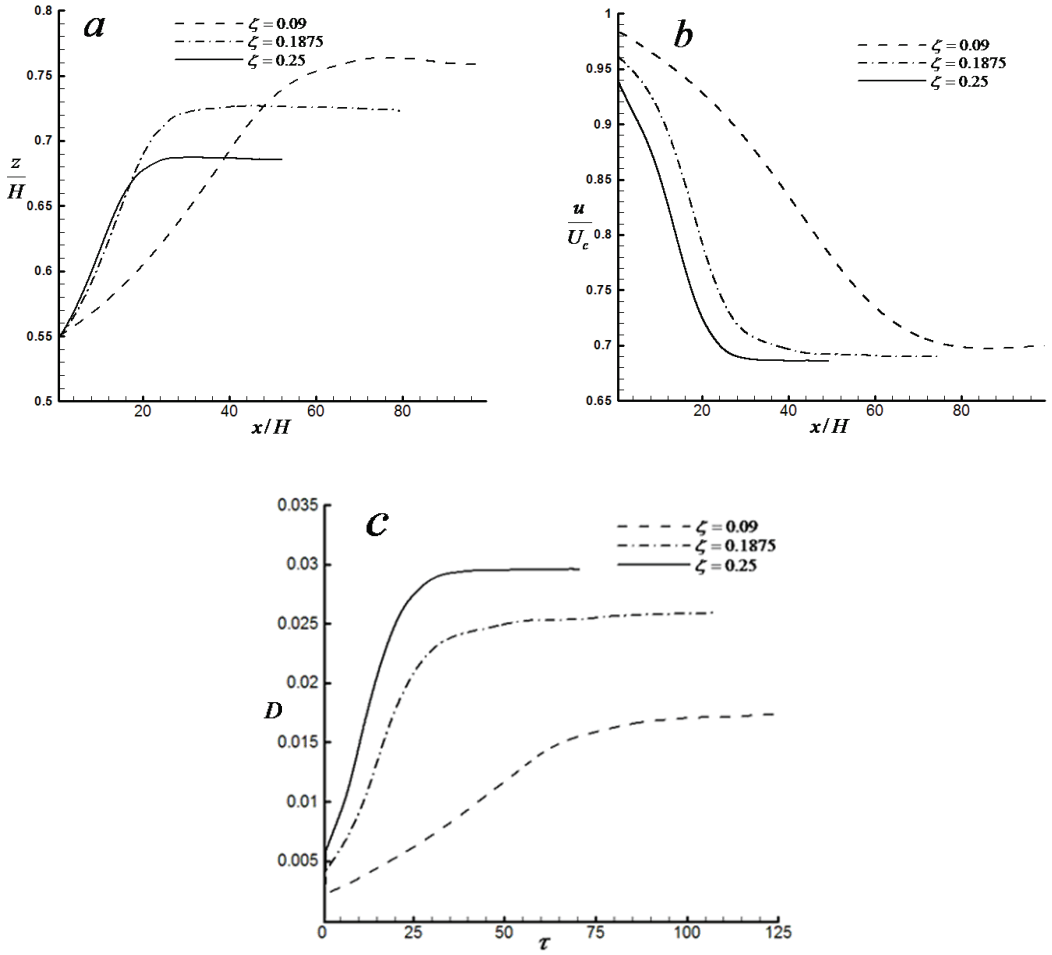

Fig. 16. (a) The lateral position, (b) axial velocity versus the axial position and (c) drop deformation versus non-dimensional time at three different drop sizes at $\mathrm{Re}_d = 10$, $Ca = 0.05$, $\alpha = \lambda = 1$

4. CONCLUSION

In the present study, finite difference/front tracking method has been used for simulation of the motion of a neutrally buoyant drop between two parallel plates in plane Poiseuille flow.

For validation of the model, the simulation was done at two low-Reynolds numbers, i.e., $\mathrm{Re}_d = 0.25$ and $\mathrm{Re}_d = 1$. The results were compared with those reached by Mortazavi & Tryggvason [15], who simulated the two-dimensional deformable drops. The results showed that the drop with $\lambda = 0.125$ migrates towards the centerline and the drop with $\lambda = 1$ migrates away from the centerline. So, at low-Reynolds numbers, the motion of a drop depends on the ratio of the drop viscosity to the viscosity of the suspending fluid. A drop with a small viscosity moves towards the centerline, but a drop with viscosity comparable to the suspending fluid moves to the wall. This effect was also observed in the Stokes flow simulations of Zhou & Pozrikidis [10].

In section 3.c, the motion of a liquid drop was studied at higher Reynolds numbers, and the effects of various governing parameters were examined. Simulation of drops with different initial positions showed that the drop that is initially close to the wall migrates towards the centerline, whereas the drop that is initially close to the centerline migrates towards the wall. Therefore, all drops with different initial positions move to an equilibrium lateral position about halfway between the centerline and the wall according to the so-called Segre-Silberberg effect. Drops with different capillary numbers were also examined. Increasing the capillary number moves the equilibrium position closer to the centerline. The axial velocity and the drop deformation increase with increasing the capillary number, which is consistent with the results of Mortazavi & Tryggvason [15] and Tsai & Miksis [27]. In this study, we found that steady-state drop shapes are obtained up to $Ca = 1$. Above this critical value of capillary number, the drop does not obtain a steady shape but instead, elongates with no limit and eventually breaks up. As the Reynolds number increases, the equilibrium position moves slightly closer to the wall, which is in agreement with the theory of Schonberg & Hinch [29] and the axial velocities decrease, whereas the slip velocities increase. With increasing Reynolds number, the drop deformation increases slightly. Increasing the viscosity ratio moves the equilibrium position slightly closer to the centerline and increases the axial velocity. The degree of deformation for steady drop shapes increases with increasing viscosity ratio, but the trends for the dynamic deformation are not as simple. With increasing the radius of the drop, the centroid of the drop moves away from the wall and the axial velocity decreases, but the degree of deformation increases.

The equilibrium position of the three-dimensional drop is close to that predicted by two-dimensional simulations. Deformation, streamlines and the variation of the equilibrium position of the three-dimensional drop with capillary number, Reynolds number, viscosity ratio and drop size agree qualitatively with two-dimensional simulations of Mortazavi & Tryggvason [15]. But the translational velocities do not agree quantitatively with two-dimensional simulations. This is due to the fact that we are considering a real drop in three-dimensional simulations, whereas in the two-dimensional case, the cylindrical sections are simulated.

REFERENCES

1. Segre, G. & Silberberg, A. (1962). Behaviour of macroscopic rigid spheres in Poiseuille flow, Part 1. Determination of local concentration by statistical analysis of particle passages through crossed light beams. *J. Fluid Mech*., Vol. 14, pp. 115-135.
2. Segre, G. & Silberberg, A. (1962). Behaviour of macroscopic rigid spheres in Poiseuille flow, Part 2. Experimental results and interpretation. *J. Fluid Mech*., Vol. 14, p. 136.
3. Karnis, A., Goldsmith, H. L. & Mason, S. G. (1963). Axial migration of particles in Poiseuille flow. *Nature*. Vol. 200, pp. 159-160.
4. Karnis, A., Goldsmith, H.L. & Mason, S. G. (1966). The flow of suspensions through tubes, Inertial effects. *J. Chem. Engng*. Vol. 44, pp. 181-193.

5. Kowalewski, T. A. (1984). Concentration and velocity measurement in the flow of droplet suspensions through a tube. *Experiments in Fluids*. Vol. 2, pp. 213-219.
6. Ho, B. P. & Leal, L. G. (1974). Inertial migration of rigid spheres in two-dimensional unidirectional flows. *J. Fluid Mech*., Vol. 65, pp. 365-400.
7. Richardson, S. (1973). Two-dimensional bubbles in slow viscous flows. Part 2. *J. Fluid Mech*., Vol. 58, pp. 115-127.
8. Griggs, A. J., Zinchenko, A. Z. & Davis, R. H. (2007). Low-Reynolds-number motion of a deformable drop between two parallel plane walls. *Int. J. Multiphase Flow*, Vol. 33, pp. 182-206.
9. Janssen, P. J. A. & Anderson, P. D. (2008). A boundary-integral model for drop deformation between two parallel plates with non-unit viscosity ratio drops. *J. Computational Physics*. Vol. 227, pp. 8807-8819.
10. Zhou, H. & Pozrikidis, C. (1994). Pressure-driven flow of suspensions of liquid drops. *Phys. Fluids*. Vol. 6, pp. 80-94.
11. Talaie, M. R., Fathikalajahi, J. & Taheri, M. (2008). Prediction of droplet dispersion and particle removal efficiency of a venturi scrubber using distribution functions. *Iranian Journal of Science & Technology, Transaction B, Engineering*, Vol. 32, No. B1, pp. 25-38.
12. Coulliette, C. & Pozrikidis, C. (1998). Motion of an array of drops through a cylindrical tube. *J. Fluid Mech*., Vol. 358, pp. 1-28.
13. Feng, D. J., Hu, H. H. & Joseph, D. D. (1994). Direct simulation of initial value problems for the motion of solid bodies in a Newtonian fluid. Part 1. Sedimentation. *J. Fluid Mech*., Vol. 261, pp. 95-134.
14. Feng, D. J., Hu, H. H. & Joseph, D. D. (1994). Direct simulation of initial value problems for the motion of solid bodies in a Newtonian fluid. Part 2. *Couette and Poiseuille flows. J. Fluid Mech*., Vol. 277, pp. 271-301.
15. Mortazavi, S. S. & Tryggvason, G. (2000). A numerical study of the motion of drops in Poiseuille flow, Part1: Lateral migration of one drop. *J. Fluid Mech*., Vol. 411, pp. 325-350.
16. Unverdi, S. O. & Tryggvason, G. (1992). A front-tracking method for viscous incompressible multi-fluid flows. *J. Comput. Phys*., Vol. 100, pp. 25-82.
17. Unverdi, S. O. & Tryggvason, G. (1992). Computations of multi-fluid flows. *Physics*, Vol. D60, pp. 70-83.
18. Tryggvason, G., Bunner, B., Esmaeeli, A., Juric, D., Al-Rawahi, N., Tauber, W., Han, J., Nas, S. & Jan, Y. J. (2001). A front-tracking method for the Computations of Multiphase Flow. *J. Computational Physics*. Vol. 169, pp. 708-759.
19. Adams, J. (1989). MUDPACK: Multigrid FORTRAN software for the efficient solution of linear elliptic partial differential equations. *Appl. Math. Comput*., Vol. 34, pp. 113-146.
20. Doddi, S. K. & Bagchi, P. (2008). Lateral migration of a capsule in a plane Poiseuille flow in a channel. *Int. J. Multiphase Flow*, Vol. 34, pp. 966-986.
21. Chan, P. C. & Leal, L. G. (1979). The motion of a deformable drop in a second-order fluid. *J. Fluid Mech*., Vol. 92, pp. 131-170.
22. Hiller, W. & Kowalewski, T. A. (1987). An experimental study of the lateral migration of a droplet in a creeping flow. *Exps. Fluids*., Vol. 5, pp. 43-48.
23. Oliver, D. R. (1962). Influence of particle rotation on radial migration in the Poiseuille flow of suspensions. *Nature*, Vol. 194, pp. 1269-1271.
24. Martinez, M. J. & Udell, K. S. (1990). Axisymmetric creeping motion of drops though circular tubes. *J. Fluid Mech*. Vol. 210, pp. 565-591.
25. Taylor, G. I. (1934). The deformation of emulsions in definable fields of flow. *Proc. R. Soc. London Ser. A*, Vol. 146, p. 501.
26. Kang, Q., Zhang, D. & Chen, S. (2005). Displacement of a three-dimensional immiscible droplet in a duct. *J. Fluid Mech*., Vol. 545, pp. 41-66.

27. Tsai, T. M. & Miksis, M. J. (1994). Dynamics of a drop in a constricted capillary tube. *J. Fluid Mech*., Vol. 274, pp. 197-217.
28. Schleizer, A. D. & Bonnecaze, R. T. (1999). Displacement of a two-dimensional immiscible droplet adhering to a wall in shear and pressure-driven flows. *J. Fluid Mech*., Vol. 383, pp. 29-54.
29. Schonberg, J. A. & Hinch, E. J. (1989). Inertial migration of a sphere in poiseuille flow. *J. Fluid Mech*., Vol. 203, pp. 517-524.
30. Yang, B. H., Wang, J., Joseph D. D., Hu, H. H., Pan, T. W. & Glowinski, R. (2005). Migration of a sphere in tube flow. *J. Fluid Mech*., Vol. 540, pp. 109-131.
31. Asmolov, E. S. (1999). The inertial lift on a spherical particle in a plane Poiseuille flow at large channel Reynolds number. *J. Fluid Mech*., Vol. 381, pp. 63-87.